Features of seafloor hydrothermal alteration in metabasalts of mid-ocean ridge origin from the Chrystalls Beach Complex

Caroline Hung[a,b*], Lisa A. Gilbert[a,b], Damon A.H. Teagle[c], Dave Craw[d] and Reinhard A. Wobus[b]

[a]The Maritime Studies Program of Williams College and, Mystic Seaport, Connecticut, USA;[b]Department of Geosciences, Williams College, Williamstown, Massachusetts, USA;[c]School of Ocean and Earth Science, National Oceanography Centre Southampton, University of Southampton, SO14-3ZH, UK; [d]Department of Geology, University of Otago, Dunedin, NZ.

*Caroline Hung: chung041@ucr.edu, +1-425-420-5258

2460 Geology, UC Riverside, 3401 Watkins Dr., Riverside, CA 92521, United States

Features of seafloor hydrothermal alteration in metabasalts of mid-ocean ridge origin from the Chrystalls Beach Complex

Abstract

The Taieri Mouth locale of the Chrystalls Beach Complex (CBC) in the South Island of New Zealand includes well preserved to strongly deformed pillow lavas. Flattened veins of epidote, quartz and chlorite intercalated with basalt flows and volcanoclastic breccias. The tectonic affinity for the rare igneous portion of the predominantly sedimentary CBC has not been well established in the context of its regional metamorphic geology. New field, petrographic, geochemical and isotopic observations suggest a mid-ocean ridge origin for the Taieri metabasalts. Further, paleo-vertical networks of epidote-quartz-chlorite veins and cross-cutting faults suggest timing of seafloor fluid-flow. Altered pillows and epidote separates have $\delta^{18}O$ isotope values ranging from 9.3 to 13.1‰. This indicates slightly enriched $\delta^{18}O$ fractionation resulting from seafloor weathering and low-temperature (<250ºC) exchange between seawater and hydrothermal fluids in basaltic fractures. Age-corrected $^{87}Sr/^{86}Sr$ ratios between 0.704135 and 0.70624 show low temperature fluid-rock interactions where the altered pillows and veins did no succumb to major mineralogic changes or isotopic re-equilibration after formation. In contrast, compressed s-fold epidote and coarse quartz veins near metasediments are suggestive of the elevated temperatures and pressures during accretion. We differentiate between episodic seafloor venting and accretional wedge-related alteration recorded within these metabasalts.

Keywords: Otago region, metabasalts; seafloor hydrothermal alteration; mid-ocean ridge processes; veins; epidote; petrology; geochemistry; trace elements; isotopic analysis; ophiolite

Introduction

The Chrystalls Beach Complex (CBC) (Nelson 1982; Coombs et al. 2000; Fagereng and Cooper 2010a,b) crops out a <1000 km^2 region on the coast in southeast Otago between Barrier Range and Dunedin. The complex comprises of deformed sub-greenschist facies greywacke, chert, and minor metabasalt in a pelitic matrix. Radiolarian fossils (Campbell and Campbell 1970) and detrital zircon ages (Adams et al. 2007) place the sedimentary protolith in the Early-Late Triassic with peak metamorphic ages in the Middle-Late Jurassic (Nishimura et al. 2000). With features such as soft sediment pull-aparts, weakly developed slaty cleavage, folds in dismembered bedding, and quartz-fibre lineated surfaces, the CBC has been interpreted to be an accretionary mélange within the Otago Schist (Fig. 1a; Nelson 1982).

Due to variable metasediment geochemistry (Coombs et al. 2000), lithologies, and U/Pb zircon ages (Adams et al. 2007), the CBC's relationship to the terranes relevant to the origin of the Otago Schist has been a discussed area of problematic affinity. Straddling in between well-studied terranes of the Otago Schist, the CBC block reported initial $^{87}Sr/^{86}Sr$ ratios intermediate to known values of the Caples and Torlesse terranes (Adams and Graham 1997). The emplacement of CBC has been referred to as an autochthonous subunit of the Caples terrane despite its silica-rich contents exhibiting greater similarity to the metasedimentary and felsic rocks of the Torlesse Terrane (Mortimer and Roser 1992). Amongst the minor igneous portions of three localities referred to as Taieri Mouth, Akatore Beach, and Watsons Beach within the CBC, normal- to enriched- mid-ocean ridge (N-MORB to E-MORB) and oceanic island (OIB) affinities have been proposed (Fig. 1b; Fagereng and Cooper 2010b, Pearce 1984).

We focus on the igneous portion of the CBC and test whether the metabasalts and in-situ alteration veins from Taieri Mouth (Fig. 1a) originated as syn-accretionary volcanism (Mortensen et al. 2010), or at a seamount or mid-ocean ridge (Fagereng and Cooper 2010b). Recent field observations of the fault distribution, structures, and fracture morphotypes around brecciated pillow margins challenge prior interpretations of the tectonic-volcanic origin and settings of fluid-flow. Closer look at the structures of veins and faulting at Taieri Mouth suggest a history of episodic fluid-rock interactions from both low-temperature seafloor alteration as well as later metamorphism related to accretion. The main purpose of this paper is to differentiate: (1) the tectonic affinities of the metabasalts, and (2) low-temperature seafloor verses metamorphic/accretionary wedge-related alteration signals from the veins based on texture and compositional variations of hydrothermal minerals as well as geochemical data including major and trace element concentrations and stable isotope compositions.

Geological setting

The Otago Schist is composed of amalgamated terranes that merged on an orogenic belt in the Mesozoic (Fig. 1a; Mortimer 2000). These terranes were exhumed from the accretionary prism formed by subduction under the paleo-Pacific Gondwana margin (Coombs et al. 1976; Mortimer 1993), and are predominantly metasedimentary, with minor intercalations of mafic rocks (Mortimer 2000). However, we focus on the metamorphosed volcanics within the CBC in this study. The metamorphic rocks grade into volcanogenic sediments of the Caples Terrane to the south and the quartzofeldspathic Torlesse Terranes to the northeast. Metamorphic grade varies from pumpellyite-actinolite to greenschist facies in the east and increases to amphibolite facies in the west (Mortimer 2000; Fig. 1a). Even though most of these rocks were subjected to similar penetrative deformation and metamorphic recrystallisation, Coombs et al. (2000) suggests that the igneous rocks within the CBC may be a separate, tectonically bounded fragment that has a different history from nearby terranes based on petrographic and geochemical data and radiolarian age determinations.

The focused locality within the CBC in this study, Taieri Mouth beach (Fig. 1b), is bounded by the Rakaia Terrane schists to the north and Caples Terrane schists to the west (Nelson 1982). The metavolcanic band within Taieri Mouth consists majorly (>90%) of deformed altered mafic rocks metamorphosed up to the pumpellyite-actinolite facies (Nelson 1982) and volcanic breccia with fractures filled with secondary minerals such as quartz, albite, epidote and chlorite. A small portion (<10%) of outcrops, however, exhibit relict primary pillow lava textures indicating subaqueous eruption and crystallisation (Fagereng and Cooper 2010b). The active Akatore Fault, one of the Otago region's most active faults for the last 15,000 years with an average slip rate of 1.3 mm/year, runs just inland of the Taieri outcrops (Litchfield and Lian 2004). Faulting from surface-ruptures and displacements as well as other tectonic events may have since influenced structural features of the studied outcrops (Taylor-Silva et al. 2019).

Methods

The studied outcrops of CBC at Taieri Mouth beach are located ~37 km south of Dunedin and were mapped and sampled in June 2018 (Fig. 2). Vein and major fault orientations were documented and tilt-corrected, which was determined for each outcrop by locating the downward-pointing "V" at the bottoms of preserved lava pillows.

Transmitted and reflected light petrography was done with a Leica DM2500P microscope. The SEM imaging and qualitative chemical analyses were completed using a FEI Scanning Electron Microscope with a set of silicate and oxide standards to quantify EDS spectra. Mineral identifications were supplemented by (Table 1) X-ray diffraction using the PANalytical X'Pert PRO MPD system at the University of Otago.

Total whole-rock major oxides and trace element concentrations were determined for 14 powdered samples by Bureau Veritas using ICP-AES and ICP-MS, respectively.

Oxygen isotope ratios were measured on 7 epidote concentrates and whole rock powders at the University of Texas at Austin, USA. Individual epidote fragments were hand-picked from bulk rock samples and crushed. Approximately 2.0 mg of material was analysed using the laser fluorination method of Sharp (1990). Samples were heated by a CO_2 laser in the presence of BrF 5 in order to produce O_2 gas, the analyte introduced into the ThermoElectron MAT 253. Garnet standard UWG-2 (δ 18 O value = +5.8‰) (Valley et al. 1995) and an in-house quartz standard Lausanne-1 (δ 18 O value = +18.1‰) were analysed along with samples to monitor the precision and accuracy of oxygen isotope analyses. δ 18 O values are reported relative to VSMOW, where the δ 18 O value of NBS-28 is +9.6‰. The precision on each oxygen isotope analysis is ±0.1‰ (1σ), based on the long-term analyses of standards. Sr isotopic compositions and Rb and Sr abundances were performed on the same 7 powdered epidote separates at the University of Southampton, UK. Concentrations were determined on a Thermo Fisher Scientific XSeries 2 ICP-MS using synthetic mixed element standards with Be, In and Re as internal standards, following standard clean dissolution methods. The powders were analysed with standard reference materials (SRM) and unknowns (PM-S and BCR-2). These standard reference materials have good agreement with GeoReM values. The mother solutions were subsampled to give approximately 1 μg Sr and the Sr isolated using ~50 μL Sr-Spec resin columns, the column blanks were <0.1 ng. The dried samples were loaded onto a single Ta filament with a Ta activator solution. $^{87}Sr/^{86}Sr$ was analyzed using static routine with amplifier rotation on a Thermo Fisher Scientific Triton Plus Thermal Ionization Mass Spectrometer with a beam size of ^{88}Sr = 2V. $^{87}Sr/^{86}Sr$ measurements were normalized to $^{86}Sr/^{88}Sr = 0.1194$. The long-term average $^{87}Sr/^{86}Sr$ for NIST SRM987 on the instrument is 0.710245 ± 0.000025 (2sd) on 161 analyses.

Field Observations

The Taieri Mouth locale of the CBC (Fig. 2) stretches about 350 m along the intertidal zone of the sandy beach, structurally above and below metasediments (Coombs et al. 2000; Nelson 1982). We divide the studied area of metabasalts and foliated schists into three zones (Fig. 2): headland (least deformed), pillow island, and deformed zone (most deformed).

The headland is a <100 m long metabasaltic outcrop that contains a major normal fault that dips at 20^{o}NE (Suppl. Fig. 1a) as well as non-foliated, fine-grained ellipsoidal lava pillows dipping at 18^{o}W with aspect ratio (V to H) ranging from ~2:1 to 3:2 (Fig. 2, 3a). A thrust fault with 5 m strike length dipping almost vertically within the pillow lavas is distinct towards the eastern side of the headland (Fig. 3a; Suppl. Fig. 1b). This lava flow structure hosts a meshed surface network of epidote veins flattened within the basalt with orientations dipping sub-vertical to vertical on the pillow bedding plane (Fig. 3b, c). Although the metabasalts here are chloritized and sheared, the main structural and alteration features of the lava flow are relatively well-preserved. Curved green epidote and chlorite-rich veins rim and cut across the pillows, and in the most concentrated zone, nearly filled up the entirety of a 2m x 2m reference square (Fig. 3a).

The pillow island is another outcrop of relict lava flow with pillows dipping similarly at 18^{o}W and separated from the headland by modern beach deposits. However, this 0.5-meter tall basaltic outcrop is placed in the intertidal with only the top cross-section of pillows exposed (Suppl. Fig. 1c, d), which makes structural observations of contacts almost impossible. Despite similarities to the headland in terms of lithology and metamorphic grade, the outcrop consists of sub-greenschist facies metabasalts with eroded interpillow materials and overall purplish veneer of physical weathering. There is no meshed network of veins on the pillow island, except for epidote veins tinged with iron oxides of sub-vertical orientations that are short (<10cm), straight, and occur commonly in parallel groupings of three or less.

At the deformed zone, the protolith consists of volcanic breccias while the structures of lava flow have been obliterated by penetrative deformation and shear. The few pillows identified dips steeply (60-65^{o}) to the northeast. The deformed zone features scattered outcrops and small caves (vary from 1-10m long, 1-5m wide). Folds from compressional deformation (Suppl. Fig. 1e) result in obscured pillow outlines, variable paleohorizontal and obliterated features. Flattened and curved epidote veins are like those experienced by the ductile deformation of metavolcanics. These deformed outcrops are north of the headland and pillow island, separated by several hundred meters of modern beach. This outcrop is in contact with metasediments, where there is apparent soft sediment mixing towards the northern edge (Fig. 2), where long, straight, macrocrystalline quartz veins ran on the microfaults.

Metabasalts

The Taieri metabasalts are predominantly pillow lavas with common mineral veins and deformation associated with sub-greenschist metamorphism with the absence of prehnite bearing assemblages .The metabasalts are sparsely vesicular, aphyric tholeiites with on average over 50% in modal abundance the primary aphanitic groundmass of plagioclase and clinopyroxene, 25% epidotes, 20% quartz, 5% chlorite, and <1% trace and accessory minerals. Diabasic igneous texture, quartz amydgules and albite twinning of plagioclase are relicts of primitive igneous characteristics preserved in lava flow samples in the headland (Suppl. Fig. 2). Secondary minerals from low-temperature hydrothermal alteration such as epidote and chlorite occur within both the groundmass and crosscutting veins (Fig. 4a). Pumpellyite, iron oxides (hematite) and sulphides (sphalerite and pyrite) are present within the cataclastic, fine-grained matrix of the pillow groundmass (Table 1; Suppl. Fig. 2). There are no interstitial carbonate sediments incorporated in the basaltic flows and pillows.

Veins

In the Taieri Mouth locality, the most prominent features of the metabasalt outcrops are well-defined veins consisting mainly of fine-grained epidote with subordinate chlorite, quartz and hematite. These crosscutting veins are flattened and deformed within the same plane of the pillow structures. The abundant epidote in the veins is distinctly different from the mineralogy of the metamorphic assemblage in surrounding metasediments, in which the secondary Ca-silicates are pumpellyite and actinolite (Fagereng and Cooper 2010a,b). These veins, and associated alteration of the adjacent rocks, are a principal focus of this study in which we differentiate their syn-metamorphic host origins and post-metamorphic alteration conditions.

Networks of veins (≥0.5 cm width) and veinlets (<0.5 cm width) have distinct generations of epidote, quartz, chlorite and hematite (Fig. 4; Table 1). The shape of the epidote, quartz, and chlorite grains in veins ranges from anhedral to euhedral with sharp, well-formed faces (Suppl. Fig. 2). At the headland, veins commonly thin perpendicularly relative to the dip of pillows. For example, measured in 30 cm increments at the headland sample grid 4-6 m (Fig. 3a), an epidote vein thins upward from 2.3 cm, to 1.4 cm, to 0.5 cm. Two-sided Wilcoxon rank sum tests for equal median (α=0.05) shows no significant difference in the median vein widths between the headland (geometric mean 0.6, median 0.5 ± std 1.5 cm) and pillow island (geometric mean 0.5, median 0.5 ± std 0.4 cm) (p=0.857). However, the median vein width (geometric mean 1.2, median 1.0 ± std 5.0 cm) of the deformed zone is significantly greater than at the headland and the pillow island, respectively (p=0.040, 0.017), which may suggest different mechanisms of fracture genesis at the deformed zone.

The tilt-corrected vein orientations are dipping predominantly vertical to subvertical at the headland and pillow island (Fig, 3b), but horizontal to sub-horizontal at the deformed zone. Two-sided Wilcoxon rank sum tests for equal median shows no significant difference in the median vein orientations after rotation to the paleohorizontal (p=0.804) between the headland (median 102 ± std 36 degrees) and pillow island (median 96 ± std 26 degrees).

There are three vein morphotypes in the Taieri metabasalt outcrops: straight (Fig. 4a), pillow margin (Fig. 4b), and radiating networks (Fig. 4c). Within a vein, distinctly bordered generations of minerals are commonly present. Straight veins (Fig. 4a) with epidote, quartz, chlorite and hematite are common in all three zones of the Taieri Mouth locality. At the headland, veins developed around pillow margins predominate with cataclastic epidote and quartz replacing the volcano glass and clay material (Fig. 4b). Most of these thin epidote veinlets are cross-cutting, but some extend off central bodies in fibrous patterns (Fig. 4c). Such networks of epidote veins are restricted to the basalt unit and absent from enclosing metasediments.

Offset and asymmetrically folded veins are morphotypes that have been structurally deformed since genesis (Suppl. Fig. 1e). Offset veins are found only at the headland and pillow island while asymmetrically folded veins, associated with thrust faulting, are most prominent in the deformed zone. While the compression of s-fold veins are penetrative in the deformed zone, those in the headland and pillow island are non-penetrative, as no spaces are observed between fabric planes in thin section.

Cross-cutting relationships

A concentrated zone of vertically dipping veins (Fig. 3a, b) at the headland outcrop fills a main normal fault structure with no offset. Cross-cutting relationships of fracture veins (Fig. 3c, 4c) and microfaults show sequences of genesis and structural changes.

An example of a sequence is outlined in Fig. 3c, where at least three distinct events are present. Stage 1 records the sub-vertical vein and the network of veinlets surrounding it. Stage 2 records the low angle normal microfault that offsets and fractures the Stage 1 vein. Stage 3 shows sub-vertical epidote-quartz-chlorite vein that cross-cuts the main features of Stage 1 and 2. Although the duration and exact timing between events are not addressed here, the relative sequence of fracturing is well-preserved: fracture genesis, sub-horizontal normal faulting, compression, and modern erosion after emplacement. In the lava flow zone of the headland, slickensides on the underside of overhanging rock of a minor thrust fault (Fig.; 3a) with an estimated throw of 1m suggest the direction of the fault slip motion is 212^{o} while the dip is 20^{o}NE relative to the modern tilt of the lava flow.

Analytical Results

Whole rock composition

Whole rock compositions of the Taieri metabasalts were plotted in the N-MORB tholeiite field on the TiO_2/Yb vs Nb/Yb, and Zr/(P_2O_5*10^4) vs TiO_2 tectonic discrimination diagram (Pearce and Cann, 1973; Fig. 5a). These data agree with previous analyses of the Taieri pillow basalts (Fagereng and Cooper 2010; Pitcairn et al. 2015). Silica content of pillows is within the 49-50% range with Al_2O_3 around 14-15% (Table 2). There is an enrichment in the Na_2O and K_2O contents above normal tholeiitic basalt values at around 4-5%. Concentrations of major elements are plotted against the MgO concentration (Fig. 6), because it has been used as indicator for the extent of basalt/seawater interaction (Mottl 1983). CaO and Na_2O concentrations correlate negatively to MgO concentration with the majority of the samples, while the TiO_2 concentration correlate positively. Fe_2O_3 concentration correlate positively with LOI (i.e., loss on ignition, which records mass of moisture and volatile material present in sample).

Relative to N-MORB, Taieri metabasalts exhibit strong enrichments in fluid-mobile alkali (K, Rb, Cs), and alkali earth elements (Ba, Sr) (Fig. 5b). Bulk samples exhibit enrichments in these fluid-mobile elements associate with low-temperature hydrothermal alteration at the headland and pillow island (Table 2), but not always at the deformed zone. The intensity and pattern of the enrichments of K, Rb, and Ba are lower for samples from the deformed zone, whereas Cs and Sr are the only elements that are enriched more than 20 times above N-MORB there. Although alkali element ratios are consistent between samples from the present study and Fagereng and Cooper (2010), Ba/Rb ratios (average 4.1) are less than half the primary igneous value of 11.3 published in Hofmann and White (1983), whereas Cs/Rb ratios (average 53.2 x 10^{-3}) are about 4 times the published value of 12.6 x 10^{-3}. Strontium content is consistent for those observed in dredged and drilled weathered basalts (Kawahata et al. 1987), but ranges widely from 70 to 4015 ppm (Table 2) regardless of the zones.

Epidote chemistry

The variation in the ratio of Fe^{3+} to Al in epidote $Ca_2(Fe^{3+}, Al)_3(SiO_4)_3(OH)$, (Suppl. Table 2) is thought to be dependent on the coupling between the immediate geochemical environment (e.g., host rock composition), temperature, source rocks fluid compositions (e.g., fO_2 and fCO_2) (Apted and Liou 1983; Caruso et al. 1988), volume of fluid flow (Hannington et al. 2003), and pressure (e.g. rate of crystallization [Arnason et al. 1993]). Epidote from each zone predominantly clusters within its own group in terms of Fe^{3+} content (Suppl. Fig. 3), but there are three outliers from the main trend, all from the deformed zone (Ps=25.3-33.6). The epidote from the headland is at the higher end of the Fe^{3+} to Al ratio (Ps=31.3-39.1) while the epidote from pillow island is at the lower end (Ps=28.5-33.1) (Coombs et al. 1976).

$\delta^{18}O$ and ^{87}Sr / ^{86}Sr stable isotopes

Data from the $\delta^{18}O$ and ^{87}Sr / ^{86}Sr stable isotopic analyses on four epidote and three metabasalt subsamples are listed in Table 3 and Table 4, respectively. In agreement with the enrichments of K, Rb, and Cs, metabasalts have higher $\delta^{18}O$ values (from 9.0 to 13.1‰) than primary MORB ($\delta^{18}O$=5.7 ‰ from Gregory and Taylor 1981; Muehlenbachs and Clayton 1976) (Fig. 7). Initial $^{87}Sr/^{86}Sr$ ratio for the Triassic-Jurassic age (i.e., set at 200 ma inferred from background literature of the CBC) of the metabasalts vary from 0.704135 to 0.705302 and for veins, range from 0.706223 to 0.70624 (Fig. 7).

Discussion

Tectonic origin

Geochemical analyses indicate Taieri pillows are N-MORB tholeiites of spreading centres (Fig. 5a; Pearce 2008). These results support prior work by Pitcairn et al. (2015) and Fagereng and Cooper (2010) at Taieri and contrasts with the pillows of seamount- or plume-affinities (i.e., E-MORB and/or OIB) from Akatore Creek and Watsons Beach of the CBC.

Structural evidence of veins may be speculated to support a MOR-origin of the metabasalts. The high concentration of vertical to sub-vertical veins in relation to the orientation of lava flow (Fig. 3a, b) may be related to on- or near-axis hydrothermal upflow. Abundant low-angle microfaults cross-cutting the vertical fractures may be more permissive of an extensional environment rather than those related to an accretionary wedge(MacLeod et al. 2002).

Alteration history

Multiple fracturing morphotypes in the Taieri metabasalts represent episodes of fracture genesis and alteration (Fig. 3c): (1) repetitive vertical to subvertical fracture genesis during hydrothermal upwelling interspersed by normal faulting as shown by radiating vein networks and cross-cutting features, and (2) fractures and deformation produced by post-seafloor metamorphism near the subduction zone and/or accretionary wedge. Morphotypes of veins resemble two possible stages of genesis and fluid flow: (1) crack initiation controlled by the crack-seal mechanism (Fig. 4a; Ramsay, 1980), fluid ascension (Fig. 4a; Connolly 1997), and thermal cooling (Fig. 4b,c; Oliver and Bons 2001), and (2) episodic fracturing and offset (Fagereng and Harris 2014) that enhanced shearing, new genesis, and alteration of old veins as well as newly propagated ones (Gillis and Sapp 1997).

Folds and faults present resulted from three separate events: (1) tectonic instability as the mid-ocean ridge evolved and spread (Macdonald 1982), (2) subduction-related metamorphism and faulting upon delamination and emplacement, and (3) normal and subsequent reverse fault motion of the entire assemblage from the Akatore Fault nearby in the late Cenozoic (Taylor-Silva et al. 2019). The major normal fault (Fig. 2, 3a) at the headland may have resulted from the extensional environment, because the concentrated, flattened vein radiations on the bedding plane are continuous across and uncompressed (as opposed to offset). Radiating vein networks (Fig. 4c) are found only at the headland and may have a genesis limited to the seafloor through thermal cracking (Oliver and Bons 2001; Vearncombe 1993). The crosscutting relationships of microfaults cemented by the assemblage of mineral characteristic of seafloor hydrothermal alteration (Fig. 3c) suggest continued extensional faulting and tilting with the development of hydrothermal veins at decreasing temperatures (e.g., decrease in epidote grain size) and increased fluid/rock ratios (Alexander et al. 1993). Had radiating networks of fractures at the headland formed in a wedge, the structural sub-vertical relationship to the lava flow may have been absent and would not have been preserved due to deformation. In contrast, the deformed zone is representative of the compression and obliteration of structures during accretion-related metamorphism with thick, compressed S-fold epidote veins and coarse quartz veins.

Geochemical characteristics of hydrothermally altered basalt

Taieri samples contain relict igneous minerals, and the metamorphic minerals albite, chlorite, quartz, epidote, pumpellyite and sulphide and oxide minerals. Bulk samples of altered basalt and veins from the headland and pillow island (Fig. 6) show elevated MgO varying from 4-8 wt.%. This may owe to the removal of Mg from solution and incorporation of Mg-rich secondary phases with a consistent prograde behaviour with increasing temperature (Mottl 1983; Seyfried 1987). The CaO and Na_2O wt.% of samples correlate almost inversely with the MgO concentrations (Fig. 6a, d). This shows a net direction of Ca and Na transport into alteration fluids during seafloor hydrothermal alteration of MORB. The anomalies, mostly from the deformed zone, may be the result of temperature kinetics and varied fluid/rock ratios following multiple episodes of chemical changes. For example, Coogan et al. (2019) addresses the increase in Na_2O and K_2O content of pillows during surface weathering of the seafloor and exchange between seafloor lavas and heated seawater in fractures. Due to the presence of iron-rich epidote veins in the altered basalts, Fe_2O_3 concentration is higher than that of MORB and lies at 4-10 wt.% (Shikazono et al. 1995; Fig. 6c). Similarly, the enrichment in TiO_2 is related to the chlorite components from hydrothermal alteration (Fig. 6b; MacLean and Kranidiotis 1987). The transport of mobile elements during low-temperature hydrothermal alteration (<400^{o}C) is required for the formation of chlorite and epidote-quartz assemblages. The major oxides trends reported here are expected in upper breccias, interflow sediments and pillow basalts that have undergone seafloor alteration and secondary mineral precipitation (Alt and Teagle 2003).

Ratios of Fe^{3+}:Al in epidote samples analysed by the quantitative SEM are categorized as the early pistacitic (Ps=0.28-0.37) variety formed at lower temperatures (i.e., 250-280 ^{o}C from Shikazono et al. 1995). This contrasts with later clinozoisite varieties with rising temperatures up to the pumpellyite-actinolite facies. Within the narrow gradation of epidote chemical compositions, epidotes sampled from different vein generations from the headland have higher Fe^{3+}:Al ratios (Suppl. Fig. 3), which may indicate short-range disequilibrium due to variably sourced episodic fluids even though the variability is small (Coombs et al. 1976). Alteration temperatures, depth and bulk and fluid compositions (e.g., fO_2, amount of fluid-rock exchange, dissolution rate) determine the thermal stability curves for epidote and clinozoisite under oxidizing conditions (Bird and Spieler 2004). Because zoisites form under higher hydrostatic pressure, the formation process for epidotes here may resemble hydrothermal conditions without the presence of high shearing stress (Holdaway 1972). Reported ratios should be evaluated with caution, because measurements are not limited in single-grain epidotes as the spectra may have overlapped with compositions from the underlying basalt groundmass.

Seafloor source of fluids

Compilation of past δ^{18}O and ^{87}Sr/^{86}Sr isotope studies on pillows and sheeted dikes sampled from DSDP Hole 504B (Kawahata et al. 1987), Troodos (Bickle and Teagle 1992; Turchyn et al. 2013), Semail (Gregory and Taylor 1981) and Jospehine (Alexander et al. 1993) ophiolites provide evidence for a fault-controlled, seafloor alteration history of the Taieri epidote and quartz veins at estimated temperatures from 220 to 405^{o}C. Both isotope systems are co-utilized to provide constraints on fluid sources and approximate hydrothermal temperatures of alteration. Compilations suggest slightly heavier compositions of δ^{18}O ranging from 10.7 to 12.7‰ for pillows on the oxic submarine weathering surface and from 4.9 to 11.3‰ for hydrothermally altered veined basalts to greenschist facies and sheeted dikes at greater depths. In this study, δ^{18}O values of 9.3 and 12.4‰ (Fig. 7; averaged for altered basalts and epidote grains, respectively, from Table 3) resemble hydrothermally altered basalt of the greenschist assemblage that has experienced subsequent surface weathering with seawater. In hydrothermal systems, the effects of isotopic fractionation between rock and heated fluids under low and high temperature conditions are opposing: low-temperature alteration (4ºC) with seawater would result in an ^{18}O enrichment compared to initial value of unaltered basalt whereas hydrothermal fluids (>200-300ºC) would result in an ^{18}O depletion (Muehlenbachs and Clayton 1976). The $\delta^{18}O$ values of the Taieri samples (Table 3) are reflective of crustal rocks above the diabase-gabbro contact (McCulloch et al. 1981) and exhibit enrichment relative to the initial MORB reservoir of $\delta^{18}O$ =5.7‰ (Muehlenbachs and Clayton 1976), which suggests the surface seawater weathering process. Epidote veins, secondary precipitates from low-temperature fluid interactions, are consistently more enriched in $\delta^{18}O$ than those of pillow basalts by about 3‰, reflecting low temperature alteration (~150ºC, Bickle and Teagle 1992).

As described by the tracer transport fluid-rock interactions model (Bickle and Teagle 1992), ridge hydrothermal systems exhibit flow regimes and patterns that change in three dimensions with time. Vein alteration can thus occur by isotopic exchange with a mixture of seawater and hydrothermal fluids of shifting compositions. Interpretations for $^{87}Sr/^{86}Sr$ compositions in Taieri rocks are based on two factors: (1) the $^{87}Sr/^{86}Sr$ ratio of seawater and derived hydrothermal fluid in rock at the time and site of alteration, and (2) the amount of heat available for alteration and its duration. The average $^{87}Sr/^{86}Sr$ ratio of fluids at mid-ocean ridges is ~0.7035 (Palmer and Edmond 1989) as a result of mixing between hydrothermal fluids ($^{87}Sr/^{86}Sr$=0.70285-0.70465), seawater ($^{87}Sr/^{86}Sr$=0.70916, but changes in geologic time), and the basaltic basement ($^{87}Sr/^{86}Sr$=0.7022-0.7033) in a compilation study of oceanic spreading centres around the world (Bach and Humphris 1999). Jurassic-Triassic seawater $^{87}Sr/^{86}Sr$ ratio has been estimated at 0.7075 (Koepnick et al. 1990; McArthur et al. 2001), so hydrothermal fluid output after fluid-rock exchange and alteration would be at a lower composition (as modelled by Antonelli et al. 2017; Bickle and Teagle 1992). In this study, $^{87}Sr/^{86}Sr$ compositions of epidote separates corrected to 200 Ma (Jurassic-Triassic boundary as a conservative age estimate for Taieri metabasalts based on Coombs et al. 1976; Mortimer 2000; Nelson 1982) are not homogeneous. Elevation in $^{87}Sr/^{86}Sr$ ratios of the epidote separates compared to altered basalts may have resulted from the infiltration of Triassic seawater with an $^{87}Sr/^{86}Sr$ ~ 0.7075 but are still rock-buffered. Further, the compositions of vein-forming fluids in the vertically dipping mesh network present in the headland are comparable to those of the s-folded veins at the deformed zone although the sample size is small in this study (Fig. 7). This attained fluid-rock equilibrium in which recharge was pervasive and not significantly channelled has been explained by Bickle and Teagle (1992), where $^{87}Sr/^{86}Sr$ profile shows only small differences between the less mineralogically altered diabase and intensely metasomatized epidosite rocks. The $^{87}Sr/^{86}Sr$ ratios in this study once again fit in the 'uncertain' affinity when compared to the Torelesse- and Caples- types in an isochrons study using $^{87}Sr/^{86}Sr$ ratios done by Adams and Graham (1997).

When the $\delta^{18}O$ and $^{87}Sr/^{86}Sr$ data are cross plotted (Fig.7), a fracture flow trajectory is present as modelled by DePaulo (2006). There is a much larger shift in $\delta^{18}O$ in comparison to Sr, which suggests that the fluid oxygen is interacting with much more of the rock volume than is the fluid Sr. This fracture flow model on the effects of matrix diffusion on isotopic exchange between fluid and rocks are typical of mid-ocean ridge hydrothermal vent fluids in contrast to porous flow in other geo-hydrological systems where the $^{87}Sr/^{86}Sr$ ratio changes rapidly longitudinally in the direction of flow with almost no change in $\delta^{18}O$.

Conclusions

In this study, we verified the MORB affinity for the Taieri metabasalts of the CBC accretionary wedge. The veins exposed at Taieri, first studied here in detail, pose important evidence for seafloor fluid flow. Preserved volcanic sections of oceanic crust show the flow structure of a seafloor hydrothermal system and the associated geochemical flux from seawater-fluid-rock interaction. We use a systematic approach based on structures, vein mineralogy as well as primary and secondary geochemistry to provide evidence for the igneous origin of the metabasalt and to differentiate between seafloor and subduction-related alteration history of the Taieri outcrops as part of the CBC:

1. The Taieri locale consists of MOR metabasalt pillows with seafloor hydrothermal alteration veins and later episodes of fractures, chemical alteration, and compressional deformation from post-seafloor metamorphism.
2. The fluid-rock alteration history and later metamorphism are recorded in veins, which filled the fractures, and pervasive amongst the metabasalts: (1) on the ridge-axis, crack initiation and propagation were controlled by structural extension and hydrothermal fluids, and (2) away from the ridge axis, alteration is dominated by compressional deformation, but minimal

$\delta^{18}O$ and $^{87}Sr/^{86}Sr$ isotopic fractionation from accretionary wedge-related metamorphic fluids.

Acknowledgements

We offer thanks to the following for their help: Erikka Olson in the field, Gemma Kerr with the XRD, Peter Crowley with quantitative SEM analyses, Nancy Piatczyc with the SEM, and Matthew Cooper from SOES with the ^{87}Sr isotope analyses. The University of Otago Geology Department hosted LAG for sabbatical. Samples are stored at Williams-Mystic; contact LAG at lgilbert@williams.edu.

Funding Details

This work was supported by a grant from the Northeast Section of the Geological Society of America.

Disclosure Statement

No potential conflict of interest was reported by the authors.

References

Adams C, Campbell H, Griffin W. 2007. Provenance comparisons of Permian to Jurassic tectonostratigraphic terranes in New Zealand: perspectives from detrital zircon age patterns. Geological Magazine. 144(4):701-729.

Adams C, Graham IJ. 1997. Age of metamorphism of Otago Schist in eastern Otago and determination of protoliths from initial strontium isotope characteristics. New Zealand Journal of Geology and Geophysics. 40(3): 275-286.

Alexander RJ, Harper GD, Bowman JR. 1993. Oceanic faulting and fault-controlled subseafloor hydrothermal alteration in the sheeted dike complex of the Josephine Ophiolite. Journal of Geophysical Research: Solid Earth. 98(B6): 9731-9759.

Alt JC, Teagle DA. 2003. Hydrothermal alteration of upper oceanic crust formed at a fast-spreading ridge: mineral, chemical, and isotopic evidence from ODP Site 801. Chemical Geology. 201(3-4):191-211.

Antonelli MA, Pester NJ, Brown ST, DePaolo DJ. 2017. Effect of paleoseawater composition on hydrothermal exchange in midocean ridges. Proceedings of the National Academy of Sciences. 114(47):12413-12418.

Apted MJ, Liou J. 1983. Phase relations among greenschist, epidote-amphibolite, and amphibolite in a basaltic system. American Journal of Science. 283(A):328-354.

Arnason JG, Bird DK, Liou JG. 1993. Variables controlling epidote composition in hydrothermal and low-pressure regional metamorphic rocks. na.

Bach W, Humphris SE. 1999. Relationship between the Sr and O isotope compositions of hydrothermal fluids and the spreading and magma-supply rates at oceanic spreading centers. Geology. 27(12):1067-1070

Bickle MJ, Teagle DA. 1992. Strontium alteration in the Troodos ophiolite: implications for fluid fluxes and geochemical transport in mid-ocean ridge hydrothermal systems. Earth and Planetary Science Letters. 113(1-2):219-237.

Bird DK, Spieler AR. 2004. Epidote in geothermal systems. Reviews in Mineralogy and Geochemistry. 56(1): 235-300.

Campbell JK, Campbell J. 1970. Triassic tube fossils from Tuapeka rocks, Akatore, south Otago. New Zealand journal of geology and geophysics. 13(2):392-399.

Caruso L, Bird D, Cho M, Liou J. 1988. Epidote-Bearing Veins in the State 2–14 Drill

Hole: Implications for Hydrothermal Fluid Composition. Journal of Geophysical Research: Solid Earth. 93(B11):13123-13133.

Connolly JAD. 1997. Devolatillization-generated fluid pressure and deformation-propagated fluid flow during prograde regional metamorphism. Journal of Geophysical Research: Solid Earth. 102(B8): 18149-18173.

Coogan LA, Daëron M, Gillis K. 2019. Seafloor weathering and the oxygen isotope ratio in seawater: insight from whole-rock δ18O and carbonate δ18O and Δ47 from the Troodos ophiolite. Earth and Planetary Science Letters. 508:41-50.

Coombs D, Landis C, Hada S, Ito M, Roser B, Suzuki T, Yoshikura S. 2000. The Chrystalls Beach-Brighton block, southeast Otago, New Zealand: petrography, geochemistry, and terrane correlation. New Zealand Journal of Geology and Geophysics. 43(3):355-372.

Coombs D, Nakamura Y, Vuagnat M. 1976. Pumpellyite-actinolite facies schists of the Taveyanne Formation near Loèche, Valais, Switzerland. Journal of Petrology. 17(4): 440-471.

DePaolo DJ. 2006. Isotopic effects in fracture-dominated reactive fluid-rock systems. Geochimica et Cosmochimica Act. 70(5): 1077-1096.

Fagereng Å, Cooper A. 2010. The metamorphic history of rocks buried, accreted and exhumed in an accretionary prism: an example from the Otago Schist, New Zealand. Journal of Metamorphic Geology. 28(9):935-954.

Fagereng Å, Cooper AF. 2010. Petrology of metabasalts from the Chrystalls Beach accretionary mélange-implications for tectonic setting and terrane origin. New Zealand Journal of Geology and Geophysics. 53(1):57-70.

Fagereng Å, Harris C. 2014. Interplay between fluid flow and fault–fracture mesh generation within underthrust sediments: geochemical evidence from the Chrystalls Beach Complex, New Zealand. Tectonophysics. 612:147-157.

Frost CD, Coombs DS. 1989. Nd isotope character of New Zealand sediments; implications for terrane concepts and crustal evolution. American Journal of Science. 289(6): 744-770.

Gillis KM, Sapp K. 1997. Distribution of porosity in a section of upper oceanic crust exposed in the Troodos Ophiolite. Journal of Geophysical Research: Solid Earth. 102(B5): 10133-10149.

Gregory RT, Taylor Jr HP. 1981. An oxygen isotope profile in a section of Cretaceous oceanic crust, Samail Ophiolite, Oman: Evidence for δ18O buffering of the oceans by deep (> 5 km) seawater-hydrothermal circulation at mid-ocean ridges. Journal of Geophysical Research: Solid Earth. 86(B4):2737-2755.

Hannington MD, Santaguida F, Kjarsgaard IM, Cathles LM. 2003. Regional-scale hydrothermal alteration in the Central Blake River Group, western Abitibi subprovince, Canada: implications for VMS prospectivity. Minerlium Deposita. 38(4): 393-422.

Hofmann AW, White WM. 1983.Ba, Rb, and Cs in the Earth's mantle. Zeitschrift fur Naturforschung A. 38(2): 256-266.

Holdaway MJ. 1972. Thermal stability of Al-Fe epidote as a function of f_{O2} and Fe content. Contributions to Mineralogy and Petrology. 37(4):307-340.

Humphris SE, Thompson G. 1978. Hydrothermal alteration of oceanic basalts by seawater. Geochimica et Cosmochimica Acta. 42(1):107-125.

Kawahata H, Kusakabe M, Kikuchi Y. 1987. Strontium, oxygen, and hydrogen isotope geochemistry of hydrothermally altered and weathered rocks in DSDP Hole 504B, Costa Rica Rift. Earth and planetary science letters. 85(4): 343-355.

Koepnick RB, Denison RE, Burke WH, Hetherington EA, Dahl DA. 1990. Construction of the Triassic and Jurassic portion of the Phanerozoic curve of seawater 87Sr/86Sr. Chemical Geology: Isotope Geoscience section. 80(4): 327-349.

Litchfield NJ, Lian OB. 2004. Luminescence age estimates of Pleistocene marine terrace and alluvial fan sediments associated with tectonic activity along coastal Otago, New Zealand. New Zealand Journal of Geology and Geophysics. 47(1):29-37.

Macdonald KC. 1982. Mid-ocean ridges: Fine scale tectonic, volcanic and hydrothermal processes within the plate boundary zone. Annual Review of Earth and Planetary Sciences. 10(1):155-190.

MacLean WH, Kranidiotis P. 1987. Immobile elements as moniotors of mass transfer in hydrothermal alteration; Phelps Dodge massive sulfide deposit, Matagami, Quebec. Economic Geologu. 82(4):951-962.

MacLeod CJ, Escartin J, Banerji D, Banks GJ, Gleeson M, Irving DHB, Lilly RM, McCaig AM, Niu Y, Allerton S, Smith Dk. 2002. Direct geological evidence for oceanic detachment faulting: The mid-atlantic ridge, 15º45'N. Geological Society of America. 30(10): 879-882.

McArthur JM, Howarth R, Bailey T. 2001. Strontium isotope stratigraphy: LOWESS version 3: best fit to the marine Sr-isotope curve for 0–509 Ma and accompanying look-up table for deriving numerical age. The Journal of Geology. 109(2):155-170.

McCulloch MT, Gregory RT, Wasserburg G, Taylor Jr HP. 1981. Sm-Nd, Rb-Sr, and 18O/16O isotopic systematics in an oceanic crustal section: Evidence from the Samail Ophiolite. Journal of Geophysical Research: Solid Earth. 86(B4):2721-2735.

Mortensen JK, Craw D, MacKenzie DJ, Gabites JE, Ullrich T. 2010. Age and origin of orogenic gold mineralization in the Otago Schist Belt, South Island, New Zealand: Constraints from lead isotope and 40Ar/39Ar dating studies. Economic Geology. 105(4):777-793.

Mortimer N. 1993. Jurassic tectonic history of the Otago schist, New Zealand. Tectonics. 12(1):237-244.

Mortimer N. 2000. Metamorphic discontinuities in orogenic belts: example of the garnet-biotie-albite zone in the Otago Schist, New Zealand. International journal of earth sciences. 89(2): 295-306.

Mortimer N, Roser BP. 1992. Geochemical evidence for the position of the Caples-Torlesse boundary in the Otago Schist, New Zealand. Journal of the Geological Society. 149(6): 967-977.

Mottl MJ. 1983. Metabasalts, axial hot springs, and the structure of hydrothermal systems at mid-ocean ridges. Geological Society of America Bulletin. 94(2):161-180.

Muehlenbachs K, Clayton R. 1976. Oxygen isotope composition of the oceanic crust and its bearing on seawater. Journal of Geophysical Research. 81(23):4365-4369.

Nelson KD. 1982. A suggestion for the origin of mesoscopic fabric in accretionary melange, based on features observed in the Chrystalls Beach Complex, South Island, New Zealand. Geological Society of America Bulletin. 93(7):625-634.

Nishimura Y, Coombs DS, Landis CA, Itaya T. 2000. Continuous metamorphic gradient documented by graphitization and K-Ar age, southeast Otago, New Zealand. American Mineralogist. 85(11-12):1625-1636.

Oliver NH, Bons PD. 2001. Mechanisms of fluid flow and fluid-rock interaction in fossil metamorphic hydrothermal systems inferred from vein-wallrock patterns,

geometry and microstructure. Geofluids. 1(2): 137-162.
Palmer M, Edmond J. 1989. The strontium isotope budget of the modern ocean. Earth and Planetary Science Letters. 92(1):11-26.
Pearce JA. 2008. Geochemical fingerprinting of oceanic basalts with applications to ophiolite classification and the search for Archean oceanic crust. Lithos. 100(1-4): 14-48.
Pearce JA, Cann JR. 1973. Tectonic setting of basic volcanic rocks determined using trace element analyese. Earth and Planetary Science Letters. 19(2):290-300.
Pearce JA, Lippard S, Roberts S. 1984. Characteristics and tectonic significance of supra-subduction zone ophiolites. Geological Society, London, Special Publications. 16(1):77-94.
Pitcairn IK, Teagle DA, Craw D, Olivo GR, Kerrich R, Brewer TS. 2006. Sources of metals and fluids in orogenic fold deoposits: insights from the Otago and Alpine Schists, New Zealand. Economic Geology. 101(8): 1525-1546.
Pitcairn IK, Craw D, Teagle DAH. 2015. Metabasalts as sources of metals in orogenic gold deposits. Mineralium Deposits. 50(3): 373-390.
Ramsay JG. 1980. The crack–seal mechanism of rock deformation. Nature. 284(5752):135.
Roser BP, Cooper AF. 1990. Geochemistry and terrane affliation of Haast Schist from the western Southern Alps, New Zealand. New Zealand Journal of Geology and Geophysics. 33(1):1-10.
Seyfried WE. 1987. Experimental and theoretical constraints on hydrothermal alteration processes at mid-ocean ridges. Annual Review of Earth and Planetary Sciences. 15(1):317-335,
Sharp ZD. 1990. A laser-based microanalytical method for the in situ determination of oxygen isotope ratios of silicates and oxides. Geochimica et Cosmochimica Acta. 54(5):1353-1357.
Shikazono N, Utada M, Shimizu M. 1995. Minerlogical and geochemical characteristics of hydrothermal alteration of basalt in the Kuroko mine area, Japan: implications for the evolution of a Back Arc Basin hydrothermal system. Applied geochemistry. 10(6): 621-641.
Sun SS, McDonough WF. 1989. Chemical and isotopic systematics of oceanic basalts: implications for mantle composition and processes. Geological Society of London, Special Publications. 42(1):313-345.
Taylor-Silva BI, Stirling MW, Litchfield NJ, Griffin JD, van den Berg EJ, Wang N. 2019. Paleoseismology of the Akatore Fault, Otago, New Zealand. New Zealand Journal of Geology and Geophysics.1-17.
Turchyn AV, Alt JC, Brown ST, DePaolo DJ, Coggon RM, Chi G, Bedard JH, Skulski T. 2013. Reconstructing the oxygen isotope composition of late Cambrian and Cretaceous hydrothermal vent fluid. Geochimica et cosmochimica acta. 123:440-458.
Valley JW, Kitchen N, Kohn MJ, Niendorf CR, Spicuzza MJ. 1995. UWG-2, a garnet standard for oxygen isotope ratios: strategies for high precision and ccuracy with laser heating. Geochimica et Cosmochimicha Acta. 59(24): 5223-5231.
Vearncombe J. 1993. Quartz vein morphology and implications for formation depth and classification of Archaean gold-vein deposits. Ore Geology Reviews. 8(5):407-424.

Tables

Table 1. Location (coordinate system of WGS1984), mineralogy, and estimated modal abundances (only for samples with thin sections made) of bulk samples. Mineralogy determined by XRD and thin section studies (see Fig. 2, 3a for sample locations).

Sample	Lat (S)	Long. (E)	Location†	Mineralogy*	Groundmass**	Quartz	Epidote	Chlorite	Oxides	Trace
2018CBMF-11	-46.073519	170.201106	H	Qtz ±Chl±Ep±Hem + Pmp	5	25	20	10	40	<1
2018CBMF-12	-46.073510	170.201087	H	Qtz ±Chl±Ep±Hem	-	-	-	-	-	-
2018CBMF-15	-46.073498	170.201830	PI	Qtz ±Chl + Pmp	60	30	0	0	10	0
2018CBMF-17	-46.073534	170.201037	H	Ep + Qtz	-	-	-	-	-	-
2018CBMF-18	-46.073511	170.201073	H	Qtz ±Chl±Hem + Pmp	-	-	-	-	-	-
2018CBMF-19	-46.073543	170.201118	H	Qtz ±Chl±Ep	60	20	10	0	10	<1
2018CBMF-20	-46.073497	170.201889	PI	Qtz ±Chl±Hem	55	15	25	0	5	0
2018CBMF-21	-46.073488	170.200953	H	Ab + Qtz ±Chl + Pmp	-	-	-	-	-	-
2018CBMF-23	-46.073468	170.200957	H	Ab + Qtz ±Chl±Ep + Pmp	80	10	0	0	10	0
2018CBMF-25	-46.073077	170.201195	DZ	Qtz ±Ep	70	20	0	5	5	0
2018CBMF-26	-46.072712	170.200706	DZ	Qtz ±Chl±Ep	55	20	0	5	10	<1
2018CBMF-31	-46.073054	170.201124	DZ	Qtz ±Chl±Ep + Pmp	-	-	-	-	-	-
2018CBMF-L04	-46.073439	170.201479	PI	Ab ±Chl±Ep±Hem	70	20	0	0	10	0

† Field zones as we defined at the Taieri Mouth locality of the CBC: H=headland; PI=pillow island; DZ=deformed zone.
*Mineral abbreviations as follows in order of appearance: Qtz=quartz, Chl=chlorite, Ep=epidote, Hem=hematite, Ab=albite, Pmp=pumpellyite
**Groundmass= fine-grained basalt groundmass of plagioclase, clinopyroxene, feldspar, epidote and vesicles of quartz

Table 2. Whole rock ICP-MS results for major, minor, and trace elements in weight percent. Samples were fused with lithium borate and digested in nitric acid for complete dissolution. Data reduction was performed using proprietary internal calibration and standardization with propriety reference material SO-19 of Bureau Veritas Mineral Laboratories. LOI is loss on ignition. Mdl stands for method detection limit while bdl stands for below detection limit. Sample names listed as 2018CBMF-##.

Sample	MDL	21	23	L4	11	12	15	17	18	19	20	25	26	31	STD-1	STD-2
Zone		H	H	PI	H	H	PI	H	H	H	PI	DZ	DZ	DZ		
Major Oxides (Wt %)																
SiO_2	0.01	49.04	50.16	48.44	61.37	52.86	48.2	64.27	55.21	48.51	55.17	86.75	60.46	61.39	60.36	60.31
Al_2O_3	0.01	15.73	14.18	15.35	14.9	14.46	14.44	11.07	15.67	15.58	14.64	4.76	12.72	12.23	14	13.96
Fe_2O_3	0.04	11.3	12.41	13.53	7.46	12.14	13.16	8.72	11.6	11.65	12.3	2.08	9.58	7.99	7.42	7.49
MgO	0.01	5.96	5.5	5.03	1.87	2.86	6.79	0.88	2.31	5.69	3.17	0.21	1.15	1.73	2.93	2.92
CaO	0.01	6.93	8.1	7.64	3.78	8.64	7.76	11.21	2.9	9.14	3.8	2.85	11.84	11.15	5.93	5.94
Na_2O	0.01	4.28	2.61	3.93	5.94	4.3	2.63	0.5	6.4	4.26	5.79	1.38	0.88	1.71	4.12	4.15
K_2O	0.01	1.08	1.36	1.18	0.85	0.1	1.68	0.04	1.26	0.06	0.29	0.05	0.07	0.09	1.33	1.32
TiO_2	0.01	1.78	1.76	1.77	1.09	1.72	1.69	0.62	1.33	1.67	1.64	0.2	0.92	1.34	0.7	0.7
P_2O_5	0.01	0.16	0.16	0.18	0.11	0.16	0.15	0.06	0.12	0.16	0.12	0.02	0.09	0.16	0.31	0.32
MnO	0.01	0.16	0.23	0.17	0.12	0.17	0.15	0.16	0.14	0.19	0.17	0.04	0.12	0.12	0.13	0.13
LOI	<5.1	3.3	3.3	2.5	2.2	2.4	3	1.9	2.9	2.8	2.7	1.5	1.7	1.8	1.9	1.9
Total	0.01	99.72	99.77	99.77	99.71	99.82	99.7	99.4	99.85	99.78	99.8	99.83	99.55	99.71	99.78	99.79
Trace Elements (ppm)																
Ba	1	91	98	43	79	22	97	22	112	15	23	12	11	7	476	473
Ni	20	49	46	48	29	44	44	bdl	39	54	49	bdl	32	44	470	467
Sc	1	47	45	47	28	43	44	18	35	44	42	6	32	35	26	26
Be	1	bdl	bdl	2	bdl	bdl	2	bdl	bdl	bdl	bdl	bdl	bdl	1	19	19
Co	0.2	93.3	64.4	69.4	86.6	61.2	100.3	60.4	54.7	70.1	77	91.6	108.1	89.5	25.2	24
Cs	0.1	0.8	1.2	1	0.8	bdl	1.3	bdl	1.7	bdl	0.2	bdl	bdl	bdl	4.5	4.7
Ga	0.5	17.2	15.2	17.8	16.9	18.7	18.3	19	18.8	16.7	13.5	5.6	18.2	18.7	16.2	15.4

Hf	0.1	3	3	2.9	2	2.6	2.9	1.1	2.4	2.7	2.9	0.3	1.4	2.3	2.9	3.2
Nb	0.1	2.8	2.8	2.5	2.4	2.8	3	1.3	2.4	2.4	2.5	<0.1	1.4	2	70.5	67.2
Rb	0.1	16.5	21.8	19.1	14.5	1.6	28.4	0.2	20.4	0.6	4.5	<0.1	0.7	0.9	19.7	19.3
Sn	1	1	bdl	1	bdl	bdl	1	bdl	bdl	1	bdl	bdl	bdl	bdl	19	19
Sr	0.5	232.6	216.2	70	547	80.1	178.2	4014.5	82.1	73.2	234.4	411.1	1959.3	1093.6	321.6	315.1
Ta	0.1	0.4	0.3	0.4	0.4	0.2	0.4	0.3	0.2	0.3	0.3	0.4	0.5	0.4	5.2	4.8
Th	0.2	0.2	0.4	bdl	bdl	0.2	bdl	bdl	bdl	0.2	0.3	bdl	bdl	bdl	13.3	13.2
U	0.1	bdl	0.2	0.1	0.2	0.2	bdl	0.1	0.2	0.1	0.1	bdl	bdl	bdl	20.4	20.5
V	8	299	285	329	218	282	329	256	266	292	218	71	300	208	163	165
W	0.5	362.9	135.2	193	465.2	182.4	445.1	427.8	150.1	152.5	223.2	825	812.1	489.2	11.1	9.8
Zr	0.1	109.2	107.3	108.2	68.1	102.3	109.6	40.6	87.1	102	107.1	13	58.2	83.5	114.7	111.3
Y	0.1	44.4	36.7	39.4	28.3	36.1	34.6	20.6	29.5	34.5	32.9	4.3	32.2	30.7	36.3	35.7
La	0.1	8.3	5.3	4.9	5.7	5.6	4.8	4	5.4	4.7	4.8	1.6	5.1	4.6	75.5	72.7
Ce	0.1	15	12.2	12.2	10.2	11.8	13.1	7.5	10.4	11.8	11.1	2.2	11	9.1	165.6	158.8
Pr	0.02	2.88	2.2	2.23	1.95	2.26	2.17	1.27	1.94	2.04	1.99	0.36	1.81	1.9	19.97	19.38
Nd	0.3	14.5	11.8	11.9	10.3	12.8	11.9	6.5	10.1	11.5	11.2	1.7	9.7	9.9	76.4	73.9
Sm	0.05	4.7	3.78	3.92	3.28	4.14	3.79	2.18	3.36	3.83	3.67	0.42	2.98	3.33	13.34	12.91
Eu	0.02	1.88	1.52	1.56	1.26	1.55	1.48	0.85	1.34	1.39	1.38	0.19	1.44	1.19	3.71	3.56
Gd	0.05	6.53	5.22	5.76	4.4	5.61	5.28	2.86	4.78	5.29	5.16	0.63	4.43	4.59	10.63	10.43
Tb	0.01	1.16	0.99	1.04	0.78	0.99	0.98	0.51	0.81	0.96	0.93	0.1	0.76	0.83	1.44	1.36
Dy	0.05	7.65	6.4	6.79	4.79	6.44	6.23	3.34	5.4	6.03	5.99	0.71	4.97	5.31	7.38	7.16
Ho	0.02	1.63	1.36	1.45	1.07	1.43	1.42	0.76	1.1	1.28	1.37	0.16	1.08	1.18	1.41	1.33
Er	0.03	4.8	4.03	4.35	3.08	3.91	3.99	2.17	3.18	3.88	4.04	0.48	3.16	3.5	3.91	3.89
Tm	0.01	0.65	0.6	0.62	0.39	0.58	0.52	0.32	0.44	0.54	0.53	0.06	0.47	0.48	0.56	0.55
Yb	0.05	4.16	3.48	4.01	2.36	3.55	3.46	1.88	2.71	3.42	3.4	0.37	2.73	3.27	3.81	3.35
Lu	0.01	0.62	0.57	0.59	0.33	0.53	0.54	0.28	0.39	0.53	0.51	0.06	0.4	0.51	0.56	0.53

Table 3. $\delta^{18}O$ stable isotope and alteration temperature results for epidote and pillow basalt separates as subsamples 2018CBMF-0XX-e or 2018CBMF-0XX-p, respectively.

Sample	Type	Location	$\delta^{18}O$ (‰)
017-e	epidote	H	12.2
			11.8
019-e	epidote	H	12.3
025-e	epidote	DZ	13.1
031-e	epidote	DZ	12.6
023-p	altered basalt	H	9.2
			9.9
024-p	altered basalt	DZ	9.0
L3-p	altered basalt	PI	9.0
			9.7

Table 4. ^{87}Sr / ^{86}Sr stable isotope results for epidote and pillow basalt separates as subsamples 2018CBMF-0XX-e or 2018CBMF-0XX-p, respectively. $^{87}Sr/^{86}Sr$ measurements were normalized to $^{86}Sr/^{88}Sr$ = 0.1194. The long-term average $^{87}Sr/^{86}Sr$ for NIST SRM987 on the instrument is 0.710245 ± 0.000025 (2 standard deviations) on 161 analyses.

Sample	Type	Location	$^{87}Sr/^{86}Sr$	[Sr] ppm	[Rb] ppm	$^{87}Sr/^{86}Sr_{(200\ Ma)}$	±2SE
025-e	epidote	DZ	0.7062352	606.2	0.899	0.706223	0.000013
017-e	epidote	H	0.704206	3947	0.563	0.704207	0.000014
031-e	epidote	DZ	0.7062408	2091	0.293	0.706240	0.000019
019-e	epidote	H	0.7062348	777.5	0.413	0.704376	0.000013
023-p	altered basalt	H	0.7062346	253.2	32.68	0.705173	0.000013
024-p	altered basalt	DZ	0.7062354	197.9	22.44	0.705302	0.000013
L3-p	altered basalt	PI	0.7062350	170	43.39	0.704135	0.000013

Supplementary Tables and Figure

Supplementary Table 1. Vein orientations from mapping efforts in each field zone. Locations are given as distance east (negative) or west (positive) from the baseline (Fig. 3).

Location	Square#	Vein-ID	Segment	Strike	Dip*	Direction	Width (cm)
CUZ (2-4 m)**	1	1		109	127	W	0.4
	1	2		90	108	W	0.2
	1	3	a	153	171	W	0
	1	3	b	153	171	W	0
	1	3	c	153	171	W	0
	1	3	d	153	171	W	0
	1	4		134	152	W	0.2
	1	5		134	152	W	0
	1	6		70	88	nan	1
	1	7	a	134	152	E	1.4
	1	8	a	134	152	E	1.8
	1	8	b	134	152	E	0.4
CUZ (0-2 m)**	2	3	e	153	171	E	0
	2	3	f	153	171	W	0.6
	2	3	g	153	171	W	0
	2	3	h	153	171	E	0
	2	3	h	153	nan	nan	0
	2	3	i	153	171	E	1.4
	2	7	b	144	162	W	1.4
	2	7	c	nan	nan	W	2
	2	7	d	nan	nan	W	0.3
	2	7	e	nan	nan	W	0.3
	2	9		194	212	E	2
	2	10		194	212	W	0.2
	2	11	a	194	212	E	0.2
	2	11	b	194	212	E	0.8
	2	12	a	194	212	E	0.2
CUZ (-2-0 m)**	3	3	j	153	171	E	0
	3	3	k	153	171	E	0
	3	12	b	194	212	E	1.4

	3	13		179	197	NE	0.9
	3	14	a	164	182	SE	1.8
	3	14	b	164	182	NE	1.4
	3	14	c	164	182	NE	1.4
	3	14	d	164	182	NE	1.4
	3	15		190	208	NW	3
	3	16		124	142	SW	0.4
	3	17		135	153	E	0.6
	3	18		114	nan	N	0.2
	3	19		114	nan	N	0.2
	3	20	a	143	161	E	0.4
	3	21		143	161	E	0.6
	3	22		143	161	E	0.5
	3	23		143	161	E	0.2
	3	24		143	161	E	0.1
	3	25		143	161	E	0.1
CUZ (-4--2 m)**	4	20	b	143	161	E	0.6
	4	20	c	143	161	SW	0.3
	4	26	a	174	192	E	
	4	26	b	174	192	E	
	4	26	c	174	192	E	0.3
CUZ (-6--4 m)**	5	26	b	174	192	E	0.8
	5	26	c	174	192	NW	0.2
	5	27		144	162	W	0.2
	5	28		144	162	W	0.3
	5	29	a	144	162	W	0.3
	5	29	b	144	162	W	0.8
	5	30		48	66	NE	0.4
CUZ (-8--6 m)**	6	31		48	66	NE	0.2
CUZ (-10--8 m)**	7	32		46	64	SE	
	7	33		60	78	NE	
	7	34		60	8	W	0.3
	7	35		60	78	NW	0.4
CUZ (4-6 m)**	8	36		159	177	NE	0.6

	8	37	a	159	177	E	2.3
	8		b	nan	nan		1.4
	8		c	nan	nan		0.5
	8	38		159	177		0.1
	8	39		150	168	E	0.2
CUZ (6-8 m)**	9	40		96	114	E	0.1
CUZ (8-10 m)**	10	1		49	19	NE	0.3
	10	2		111	20	NE	0.3
CUZ (10-12 m)**	11	3		114	21	NE	0.3
	11	4		114	22	SE	0.3
headland	4	1	a	138	156	NW	0.4
	4	1	b	nan	nan		0.7
	4	2		144	162	E	0.8
	4	3		114	132	W	0
	4	4	a	150	168	E	1.4
	4	4	b	124	142	E	0.6
	4	5		138	156	E	0.8
	4	6		115	nan	nan	0.8
	4	7		164	182	NW	1.2
	4	8	a	149	167	NW	2
	4	8	b	149	167	NW	0.4
	4	8	c	149	167	NW	0
	4	8	d	149	167	NW	0.8
	4	8	e	149	167	NW	0.3
headland	5	1		139	157	NE	0.2
	5	2		129	147	NE	0.1
	5	3		156	174	NE	0.1
	5	4		156	174	NE	0.1
	5	5		119	nan	S	0.2
	5	6		75	nan	S	0.3
	5	7		154	172	NE	0.1
	5	8		128	146	SW	0.3
	5	9		97	115	SW	0.5
	5	10		136	154	NE	0.2
	5	11		173	191	E	0.3

pillow island	1	1		112	112	W	1
	1	2		106	106	W	0.8
	1	3		114	114	W	1
	1	4		109	109	W	0.25
	1	5		109	109	W	0.25
	1	6		109	109	W	0.25
	1	7		109	109	W	0.25
	1	8		109	109	W	0.25
	1	9		108	108	W	0.5
	1	10		108	108	W	0.5
	1	11		108	108	W	0.5
	1	12		103	103	W	1
pillow island	2	1		106	106	S	1
	2	2		105	105	SW	1
	2	3		123	123	SW	0.8
	2	4		136	136	W	0.5
	2	5		136	136	W	0.5
	2	6		126	126	SW	1
pillow island	3	1		95	95	NE	0.3
	3	2		92	92	NE	0.3
	3	3		153	153	SW	2
	3	4		100	100	SW	1
	3	5		116	116	SW	0.3
	3	6		127	127	NE	0.3
	3	7		194	194	SW	0.5
	3	8		119	119	SW	0.2
deformed zone	6	1	a	110	163	N	6
	6	1	b	24	175	NE	2.3
	6	2		110	179	E	1.1
	6	3		144	17	E	1
	6	4		133	163	E	1.3
	6	5		150	19	SE	1.2
	6	6		120	25		0.1
	6	7		30	157	SE	0.3
	6	8		110	13	E	0.4

	6	9		84	147	N	0.8
deformed zone	7	1	a	10	172	E	14
	7	1	b	60	142	N	15
	7	1	c	10	172	E	11
	7	2		110	142	NW	1
	7	3		144	140	NW	0.1
	7	4		133	nan	NW	0.8
	7	5		150	nan	NW	0.8

*Dip is corrected with respect to the tilt of the presiding block (i.e., if dip direction is W, + degree; if dip direction is E, 180 - degree; Table 1.)

** The CUZ (concentrated upflow zone) is referred to mapped cross-section of the lava flowat the headland in Fig. 3a.

Supplementary Table 2. Quantitative SEM results for spot epidote chemical analysis organized by sample. The numbers represent the atomic number of each element in the chemical formula of epidote $Ca_2(Fe^{3+},Al)Al_2[SiO_4][Si_2O_7]O(OH)$.

Sample	Oxide percent (%)								Calculated formula stoichiometry based on oxygen							
2018CBMF-015	Ep1	Ep2	Ep3	Ep4	Ep5	Ep6	Ep7		Ep1	Ep2	Ep3	Ep4	Ep5	Ep6	Ep7	
Ca	9.64	9.38	9.56	9.53	9.53	9.44	9.72		1.98	1.92	1.96	1.95	1.95	1.93	1.99	
Fe	4.19	4.6	4.52	4.44	4.13	4.41	4.82		0.86	0.94	0.93	0.91	0.85	0.9	0.99	
Al	10.26	10.06	10.02	10.22	10.36	10.09	9.76		2.1	2.06	2.05	2.09	2.12	2.06	2	
Si	14.77	14.71	14.76	14.67	14.77	14.89	14.63		3.03	3.01	3.02	3.01	3.03	3.05	3	
O	61.01	61.03	61.02	61	60.99	61.08	60.98		12.5	12.5	12.5	12.5	12.5	12.5	12.5	
2018CBMF-017	Ep1	Ep2	Ep3	Ep4	Ep5	Ep6	Ep7	Ep8	Ep1	Ep2	Ep3	Ep4	Ep5	Ep6	Ep7	Ep8
Ca	9.36	9.74	9.05	9.56	9.4	9.48	9.69	9.17	1.92	2	1.85	1.96	1.93	1.95	1.99	1.88
Fe	4.6	5.04	4.79	4.88	4.9	5.1	5.11	4.96	0.94	1.03	0.98	1	1	1.05	1.05	1.02
Al	10.09	9.48	10.05	9.88	9.77	9.67	9.54	9.78	2.06	1.94	2.05	2.02	2	1.99	1.96	2
Si	14.71	14.65	14.81	14.58	14.67	14.48	14.61	14.74	3.01	3	3.03	2.99	3.01	2.97	2.99	3.02
O	61.08	61	61.14	60.99	60.98	60.88	60.98	61.04	12.5	12.5	12.5	12.5	12.5	12.5	12.5	12.5
2018CBMF-019	Ep1	Ep2	Ep3	Ep4					Ep1	Ep2	Ep3	Ep4				
Ca	9.66	9.63	9.89	9.71					1.98	1.97	2.03	1.99				
Fe	5.08	5.03	4.93	5.36					1.04	1.03	1.01	1.1				
Al	9.49	9.53	9.6	9.37					1.94	1.95	1.97	1.92				
Si	14.71	14.71	14.59	14.49					3.01	3.01	2.99	2.97				
O	61	61	60.94	60.94					12.5	12.5	12.5	12.5				

2018CBMF-020	Ep1	Ep2	Ep3	Ep4	Ep5	Ep6	Ep7	Ep8	Ep9	Ep1	Ep2	Ep3	Ep4	Ep5	Ep6	Ep7	Ep8	Ep9
Ca	9.59	9.67	9.48	9.4	9.53	9.78	9.71	9.49	9.36	1.96	1.98	1.94	1.92	1.95	2.01	1.99	1.94	1.93
Fe	5.48	5	4.93	4.85	5.27	5.02	5.69	5.18	6.8	1.12	1.02	1.01	0.99	1.08	1.03	1.17	1.06	1.40
Al	9.15	9.54	9.55	9.72	9.31	9.6	8.86	9.51	8.61	1.87	1.96	1.96	1.99	1.91	1.97	1.82	1.95	1.77
Si	14.66	14.73	14.83	14.87	14.71	14.5	14.63	14.63	13.64	3.00	3.02	3.04	3.04	3.01	2.98	3.00	3.00	2.81
O	61.02	60.99	60.99	61.08	61.04	60.89	60.99	61.01	60.69	12.50	12.50	12.50	12.50	12.50	12.50	12.50	12.50	12.50
2018CBMF-025	Ep1	Ep2	Ep3	Ep4						Ep1	Ep2	Ep3	Ep4					
Ca	8.46	7.81	9.4	9.56						1.71	1.571	1.93	1.96					
Fe	3.59	3.49	4.63	4.65						0.73	0.70	0.95	0.95					
Al	8.55	8.19	10.08	9.85						1.73	1.65	2.06	2.02					
Si	17.49	18.33	14.69	14.58						3.54	3.69	3.01	2.99					
O	61.8	62.1	61.03	61.02						12.5	12.5	12.5	12.5					
2018CBMF-026	Ep1	Ep2	Ep3	Ep4						Ep1	Ep2	Ep3	Ep4					
Ca	8.75	9.7	9.58	8.85						1.78	1.99	1.96	1.81					
Fe	4.56	4.39	4.9	4.75						0.93	0.9	1	0.97					
Al	9.16	10.04	9.7	9.83						1.86	2.06	1.99	2.01					
Si	15.98	14.72	14.73	14.98						3.25	3.02	3.02	3.06					
O	61.43	60.99	61.02	61.14						12.5	12.5	12.5	12.5					

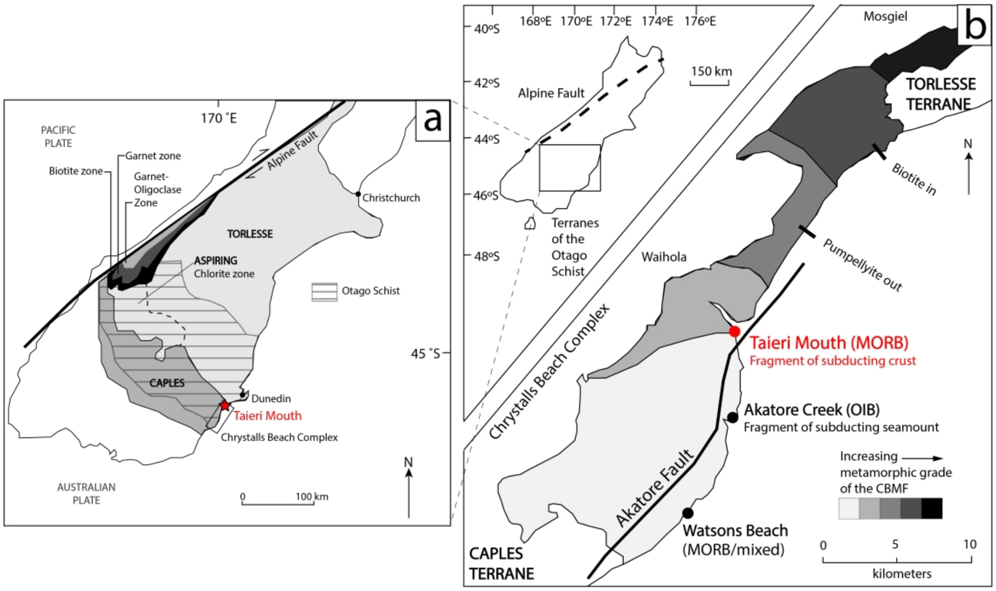

Figure 1. The tectonic origin and alteration history of the Taieri Mouth volcanics were considered within the geologic context of the Otago Schist region. a Regional map of the Otago Schist and surrounding terranes. b Location of the field site Taieri Mouth along with the studied igneous regions of the Chrystalls Beach Complex (CBC) in South Island, New Zealand. Isograds and tectonic affinities after Coombs et al. (2000), Fagereng and Cooper (2010), and Pitcairn et al. (2006).

368x219mm (300 x 300 DPI)

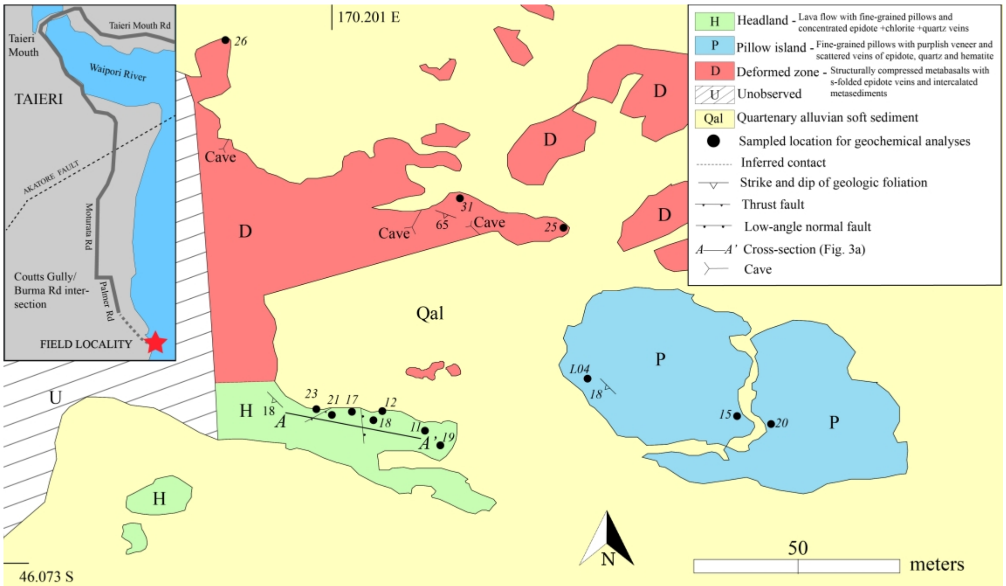

Figure 2. Geological map of the three studied zones and unobserved area (i.e., recent sediment and foliage) within the Taieri Mouth locale. Sample locations are marked with associated identification numbers. Inset shows the studied locality with respect to local roads and the Akatore Fault.

380x224mm (300 x 300 DPI)

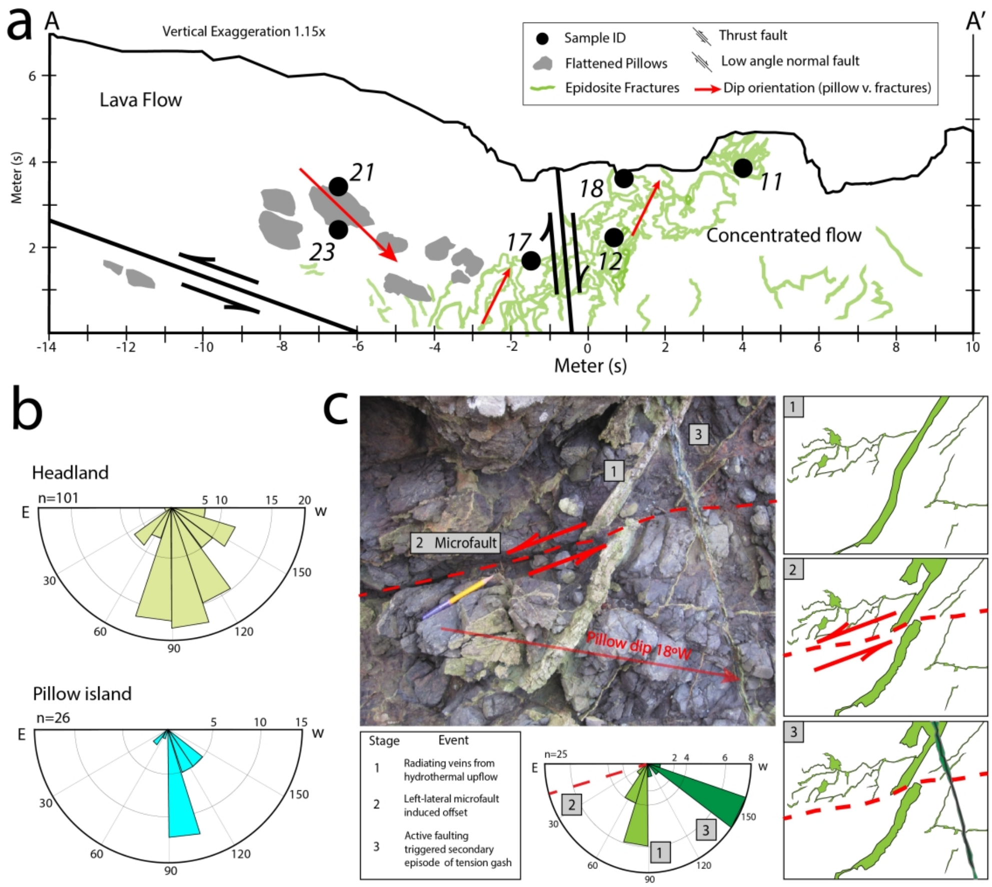

Figure 3. Structural features of pillows and veins at the headland. a Mapped cross-section of metabasalts and concentrated vein networks at the headland (24m wide outcrop; see Fig. 2) where the majority of dip orientations of veins are near perpendicular to those of pillows. b Vein dip orientation within the Headland and pillow island. The number of veins is denoted as n.c Relative sequence of fracture genesis, fluid-flow and alteration extrapolated from relict cross-cutting relationships. Restoration depicts episodic stages (1-3) of left-lateral faulting that produced the overlapping veins and microfaults. The extensional low angle normal fault of stage 2 is nearly perpendicular to the alteration veins.

261x233mm (300 x 300 DPI)

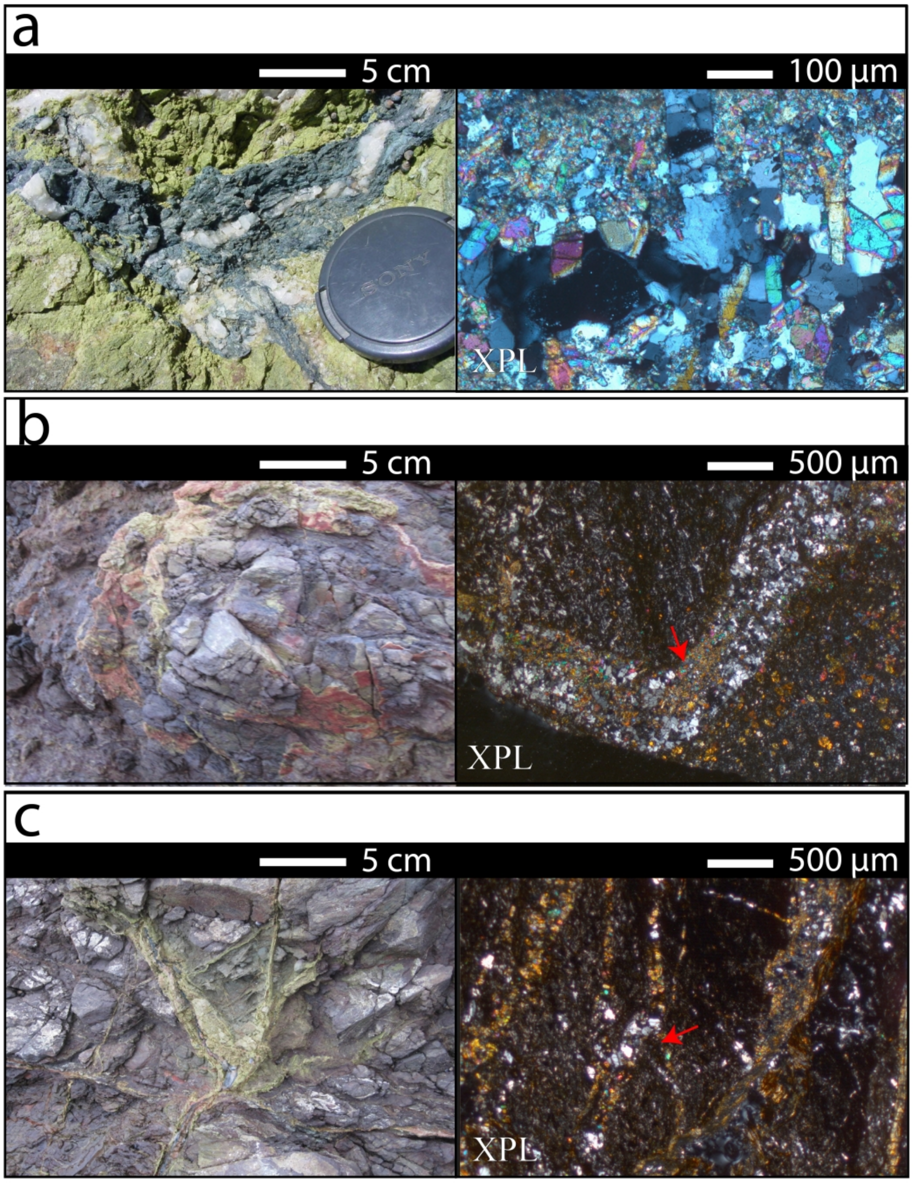

Figure 4. Vein morphotypes (left: field; right: photomicrograph) on the headland are indicative of on-axis fracture genesis: a tension gash of a straight vein, b vein around the pillow margins, and c radiating network of veins and veinlets.

276x357mm (300 x 300 DPI)

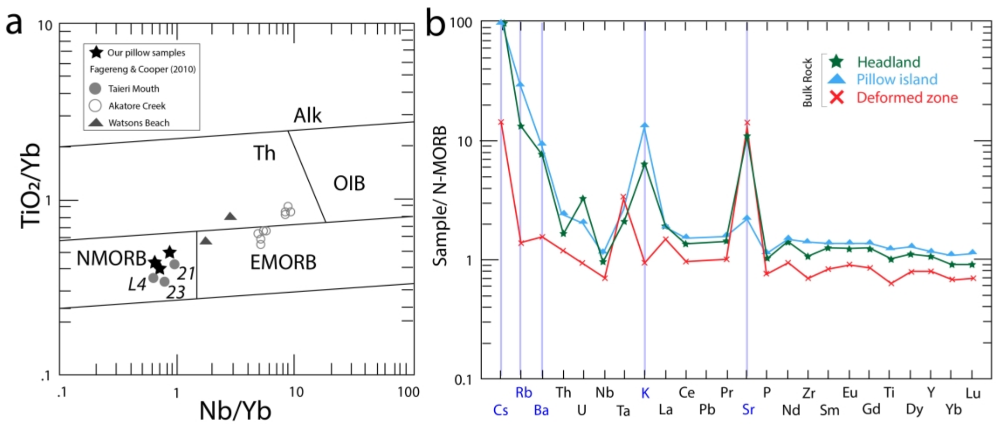

Figure 5. Major oxides and trace element results: a Pillow samples of Taieri Mouth from our studyand Fagereng & Cooper (2010) plot as mid-ocean ridge basalt (MORB) while those of Akatore Creek and Watsons Beach from Fagereng & Cooper (2010) plots as others in the tectonic discrimination diagrams N-after after Pearce (2008). . See Fig. 1 for sample location of data from Fagereng & Cooper (2010). b Trace elements of bulk rock samples from Taieri Mouth show the elemental enrichments relative to N-MORB after Sun and McDonough (1989). Blue text and lines emphasize mobile large ion lithophile elements Cs, Rb, Ba, K, Sr.

358x150mm (300 x 300 DPI)

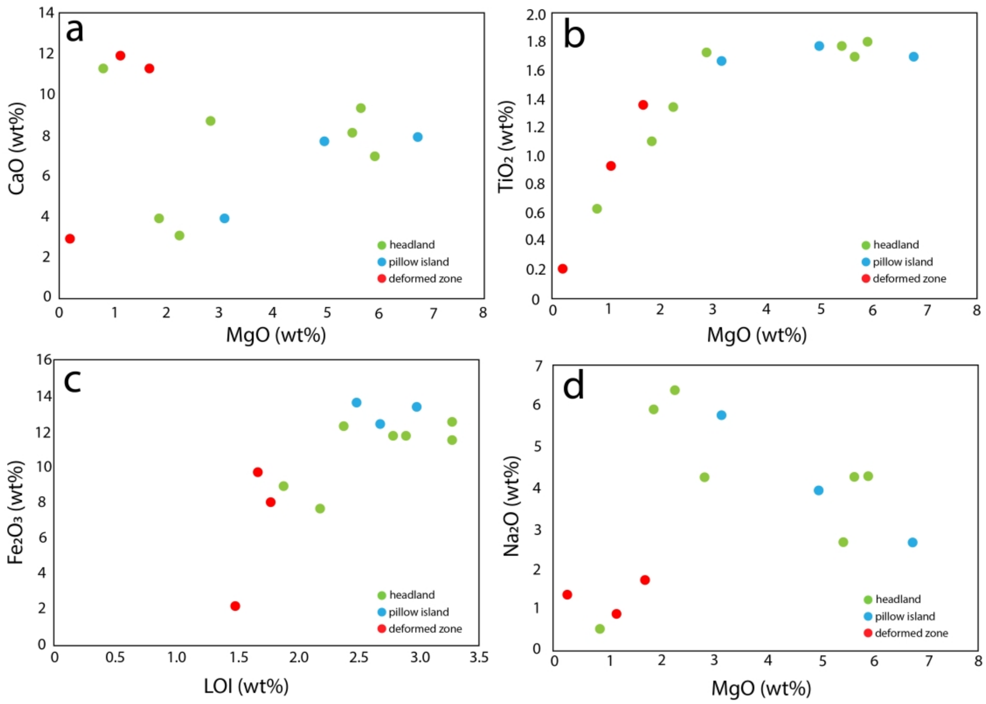

Figure 6. Major oxide relationships from bulk chemical analyses of metabasalts from the headland (green), pillow island (blue), and the deformed zone (red). These plots have been used in existing literature (Mottl 1983; Humphris and Thompson, 1978; Coogan et al., 2019) to express the extent of chemical exchange between seawater and basalt during hydrothermal alteration: a CaO v. MgO (wt. %), b TiO2 v. MgO (wt. %), c Fe2O3 v. LOI (wt. %), and d Na2O v. MgO (wt. %).

309x217mm (300 x 300 DPI)

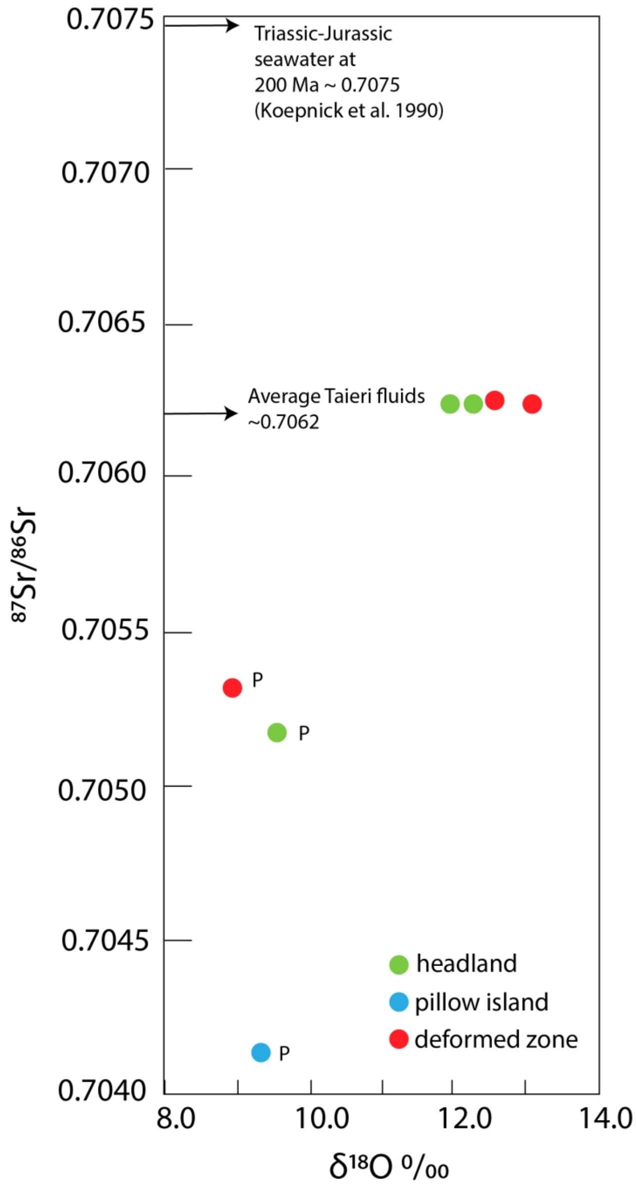

Figure 7. New 87Sr/86Sr of altered basalt and epidote grain separates corrected to 200 Ma plotted against δ18O of the same samples.

139x257mm (300 x 300 DPI)

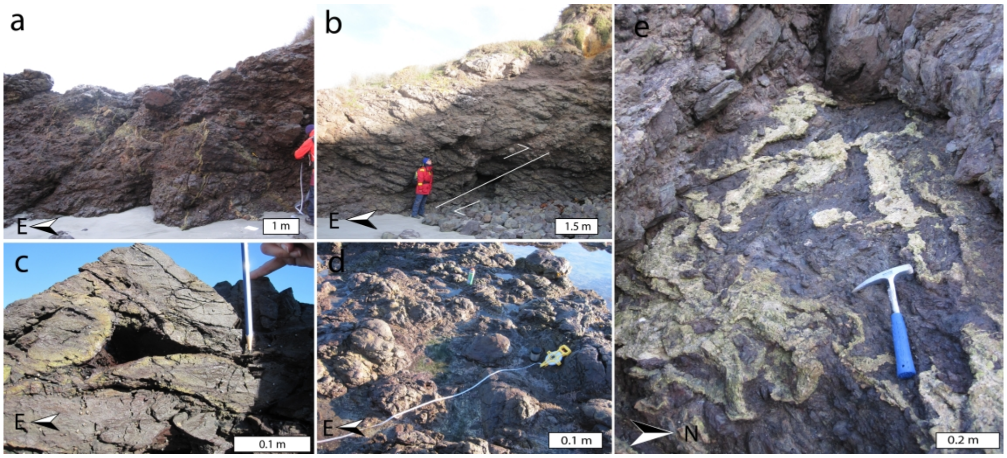

Supplementary Figure 1. Distinguishing structural features from each zone. a The headland consists of a concentrated zone of vertical veins. b The headland begins inland with a thrust fault and lava flow. c Pillows at the pillow island are surrounded by zones of weaknesses where interpillow hyaloclastites have been weathered away. d Rounded pillows on the horizontal cross-section of pillow island. e Veins in the deformed zone are compressed compared to those well-preserved at the headland.

449x202mm (300 x 300 DPI)

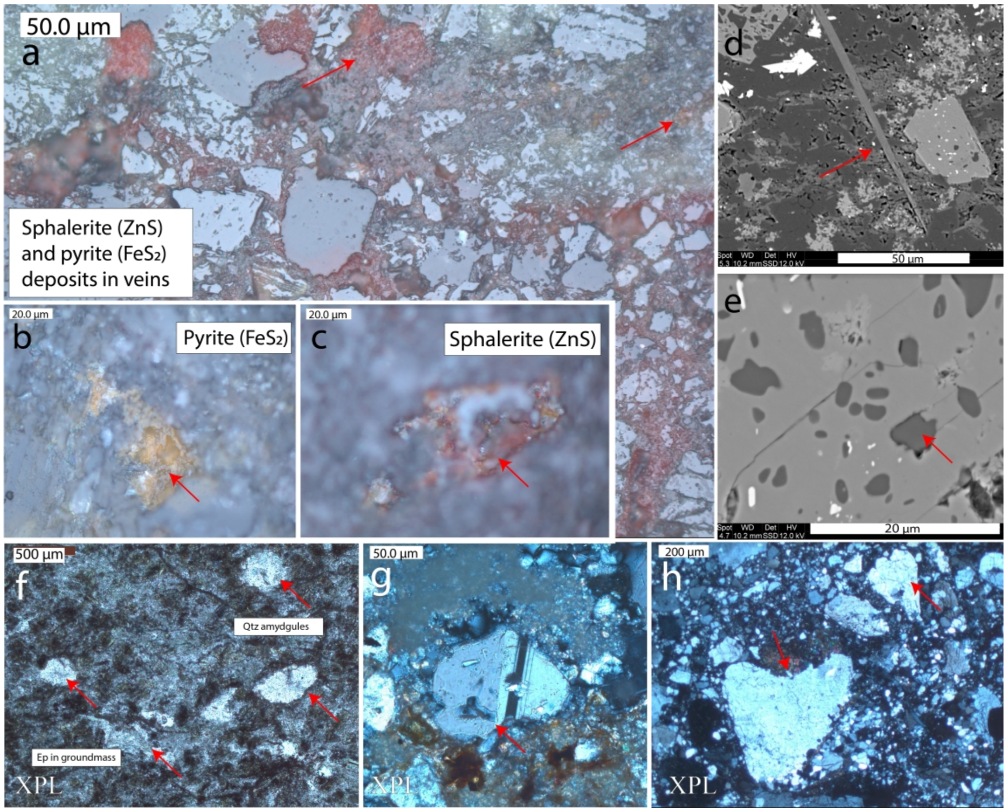

Supplementary Figure 2. Cataclastic fabrics and textures in sampled pillows are associated with low temperature (250-300oC) seafloor hydrothermal alteration. For example, reflected light microscopy shows a sulfides in the cataclastic texture of the basalt, b pyrite (yellow), and c sphalerite (red to orange). SEM shows secondary mineral replacement textures such as d an euhedral spear of epidote growth, and e the poikilitic texture of the albitization reaction in plagioclase to produce epidote. Microscopy shows f preserved quartz amydgules in basalt groundmass, g albite twinning in groundmass of plagioclase and pyroxene, h deformed grains with lack of prograde chemical changes, and the lack of carbonates.

460x370mm (300 x 300 DPI)

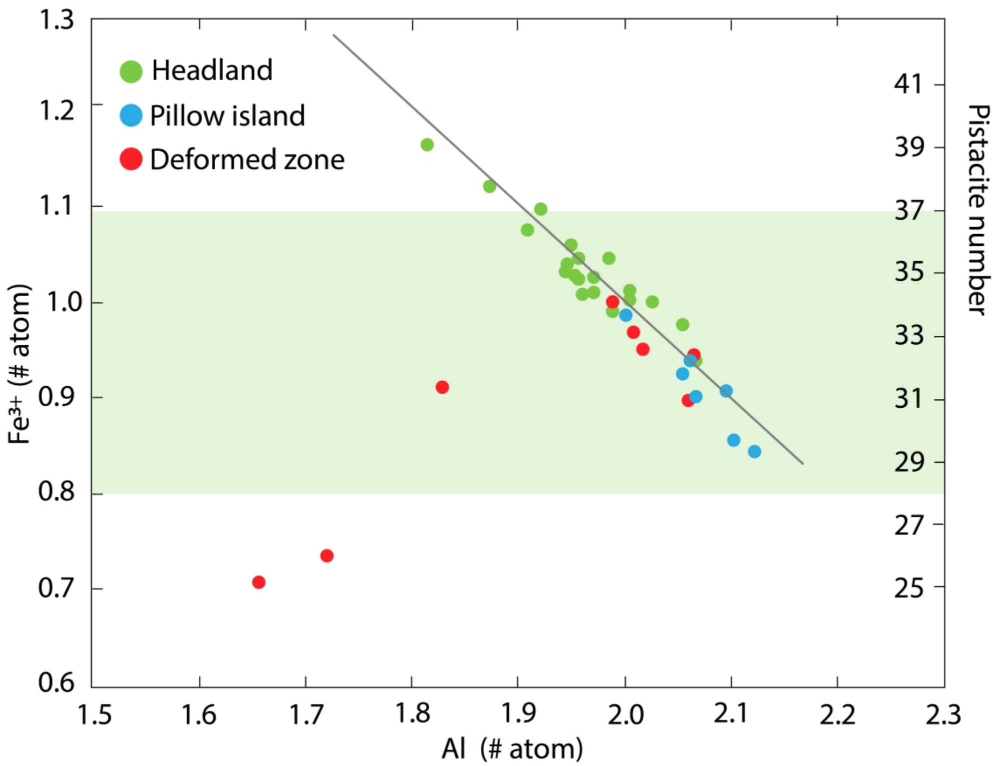

Supplementary Figure 3. Quantitative SEM data show the compositional variation in the Fe3+:Al ratio of epidote samples from the headland (green), pillow island (blue) and the deformed zone (red). Left y-axis show the pistacite number calculated by 〖Fe〗^(3+)/((〖Fe〗^(3+)+Al))×100. Grey line shows the slope governed by the stoichiometry of Fe3+ and Al atoms in epidote, which adds up to the sum of three. Green region shows the range for the early pistacitic (Ps=0.28-0.37) epidote variety.

317x244mm (300 x 300 DPI)